Journal of the Taiwan Institute of Chemical Engineers 134 (2022) 104350

Contents lists available at ScienceDirect

Journal of the Taiwan Institute of Chemical Engineers

journal homepage: www.elsevier.com/locate/jtice

Bimetallic-doped Zeolitic imidazole framework-derived Cobalt-Nitrogen-Carbon supported on reduced graphene oxide enabling efficient microwave absorption

Qi Chen[a,b], Xiaogang Su[e], Xing Liu[b], Jichao Wang[a,b], Rongguo Song[b,d], Daping He[d], Somboon Chaemchuen[a,*], Francis Verpoort[a,b,c,*]

[a] State Key Laboratory of Advanced Technology for Materials Synthesis and Processing, Wuhan University of Technology, Wuhan 430070, China
[b] School of Materials Science and Engineering, Wuhan University of Technology, Wuhan 430070, China
[c] National Research Tomsk Polytechnic University, Lenin Avenue 30, 634050 Tomsk, Russian Federation
[d] Hubei Engineering Research Center of RF-Microwave Technology and Application
[e] School of Materials Science and Engineering, North University of China, Taiyuan 030051, China

ARTICLE INFO

Article History:
Received 14 February 2022
Revised 22 March 2022
Accepted 8 April 2022
Available online 15 April 2022

Keywords:
Reduced graphene oxide
Metal-nitrogen-carbon
Poly-dcpd
Microwave absorption
Impedance matching

ABSTRACT

Background: A bimetal (Fe/Ni) doped cobalt-nitrogen-carbon matrix (Fe/Ni-CoNC) with hierarchical architecture originating from zeolitic imidazolate framework (ZIF-67) is purposely designed.
Methods: The metals within the Co-N-C matrix are well distributed. Besides, Fe/Ni-CoNC was supported on reduced graphene oxide (RGO). We demonstrate that the three-element combination can synergistically contribute to different advantages for microwave absorption. Therefore, the combination of Fe and Ni synergized the absorber to obtain a good impedance match for the best microwave absorption.
Significant Findings: The synthesized Fe/Ni-CoNC/RGO with optimized element components exhibited an excellent wave absorption of -51.6 dB at 7.2 GHz obtained with a thin thickness of 2.5 mm. When combining Fe/Ni-CoNC/RGO with a thermoset resin, namely polydicyclopentadiene (PDCPD), the final product reached a maximum absorption of -24.5 dB with a thickness of 1.5 mm. This compounding confirmed that interfacial polarization, defect polarization, and natural resonance are synchronously enhanced for improved absorption performance.
© 2022 Taiwan Institute of Chemical Engineers. Published by Elsevier B.V. All rights reserved.

1. Introduction

The rapid development of electromagnetic devices such as microwave ovens, smartphones, laptops, televisions, etc., profoundly changes the human lifestyle. They evoke transformation of traditional heat mode and instant spreading of information. However, excessive electromagnetic exposure brings severe electromagnetic interference (EMI) and electromagnetic radiation, firmly harming the other working electromagnetic devices and human health, particularly adverse to pregnant women [1]. Hence, the development of microwave absorbents with high absorption properties has become a key solution to the problem.

Generally, the performance of microwave absorbents is determined by the electrical and magnetic losses, which consume the energy of the electromagnetic wave [2]. Carbon materials are one kind of the most promising absorbents because of their high electrical losses and low density [3]. Furthermore, the graphene research [4–6], typically such as reduced graphene oxide (RGO) [7,8], has demonstrated that dipoles polarization loss is generated by the π electrons, which are vertically distributed on the RGO surface, under the action of an electromagnetic field. RGO can mainly introduce defect polarization relaxation and electron dipole relaxation of residues, which are conducive to electromagnetic waves' penetration and absorption [9–11]. Nonetheless, the pure carbon materials may lead to high permittivity and mismatching impedance, which are difficult for the materials to have ideal absorptions in the 2–18 GHz frequency range. Therefore, there is an urgent need for lowering the permittivity and increasing the permeability of carbon materials [12]. According to the impedance matching rule, introducing magnetic particles into RGO has attracted much attention as a solution. Lately, compositing transition metals with carbon materials exhibited unusual activity and stability in microwave absorption fields. The carbon layers can acquire electrons from metal particles and hinder transition metal particles from aggregation. In addition,

* Corresponding authors at: Francis Verpoort, State Key Laboratory of Advanced Technology for Materials Synthesis and Processing, Wuhan University of Technology, Wuhan, 430070, China. Somboon Chaemchuen, State Key Laboratory of Advanced Technology for Materials Synthesis and Processing, Wuhan University of Technology, Wuhan, 430070, China.
E-mail address: francis@whut.edu.cn (F. Verpoort).

https://doi.org/10.1016/j.jtice.2022.104350
1876-1070/© 2022 Taiwan Institute of Chemical Engineers. Published by Elsevier B.V. All rights reserved.

ferromagnetic metals [13] such as Co, Fe, and Ni, together with their alloys [14–16], can increase magnetic permeability and magnetic tangent loss. Their metal oxides have the positive effect of reducing permittivity to obtain better impedance matching. Especially, $NiFe_2O_4$ [17] has low coercivity, large saturation magnetization, and broadens the absorption band width, which is meaningful for improving microwave absorption. Those magnetic compounds display excellent wave absorption performances, thus significantly enhancing the material's wave absorbing ability.

Metal-organic frameworks (MOFs) [18] possess superior properties such as high surface area, excellent porosity, low density, and good permittivity [19], which makes MOFs become a good candidate for high-quality wave absorbers [20–22]. Zeolitic imidazolate framework-67 (ZIF-67) [23, 24], a sub-family of MOF materials, is constructed from cobalt ions connected with 2-methyl imidazole ligands extended in a 3D structure generating a rhombic dodecahedron crystal shape. Interestingly, the pyrolysis of ZIF-67 as a precursor produces cobalt nanoparticles in a nitrogen-carbon matrix (CoNC) which delivers an excellent microwave absorption behavior. Also, the MOF-derived carbonaceous Co/C nanocomposite showed a maximum absorption of −35.3 dB, with an absorber thickness of 4 mm [25].

In this work, we further demonstrate that by bimetallic doping of ZIF-67 using Fe and Ni, followed by mixing with reduced graphene oxide (RGO) and pyrolysis, the derived Fe/Ni-CoNC/RGO composite exhibits a significant enhancement of the microwave absorption capacity. The results indicate that compositing Fe/Ni-CoNC/RGO with dicyclopentadiene (DCPD), the composite achieved the highest absorption of −24.5 dB with a thin thickness.

2. Experimental section

2.1. Materials and reagents

Cobalt nitrate hexahydrate ($Co(NO_3)_2{\cdot}6H_2O$; ≥ 99.0%), 2-methylimidazole (2-MIM; 98.0%), Nickel(II) acetate tetrahydrate ($Ni(CH_3COO)_2{\cdot}4H_2O$; ≥99.0%), and GENAPOL(R) X-080 (wetting agent) were purchased from Sigma-Aldrich Co., Ltd. Paraffin with ceresin (melting point 62–64 °C), Trichloro(phenyl)silane ($C_6H_5Cl_3Si$; 98%), Iron(II) acetate ($Fe(CH_3COO)_2$; > 90.0%) were provided by Aladdin Co., Ltd. Methanol (CH_3OH; AR; ≥ 99.5%), Dichloromethane (CH_2Cl_2; AR; ≥ 99.5%) were obtained from Sinopharm Co., Ltd. Graphene Oxide (Diameter: 500 nm-5 μm; Thickness: 0.8–1.2 nm; single layer ratio ~ 99%; purity > 99 wt%) was purchased from Shanghai Naford Biological Technology Co., Ltd. All the chemicals were directly used without further purification. Guang Ming Chuang Xin Co kindly provided ruthenium catalyst and DCPD (dicyclopentadiene).

2.2. Material preparation

Synthesis of ZIF-67

ZIF-67 was typically synthesized from a mixture of solution A containing $Co(NO_3)_2{\cdot}6H_2O$ (0.291 g, 0.1 mmol) dissolved in methanol (13.5 mL) and solution B containing 2-methylimidazole (0.66 g, 0.8 mmol) in methanol (13.5 mL). The mixture solution was vigorously stirred at ambient temperature for 24 h before separating the solid product via centrifugal at 9000 rpm for 10 min. The purple solid was washed with methanol several times (> 3 times) until the solvent was colorless. The collected purple solid was dried at 50 °C under vacuum overnight before storing the product for further use.

Synthesis of M@ZIF-67

M@ZIF-67 (*M* = Fe and/or Ni) was synthesized using a post-synthetic method via immersion of ZIF-67 in the metal precursor solution. ZIF-67 (200 mg) was transferred in precursor solution of Fe $(CH_3COO)_2$ (50 mg) or $Ni(CH_3COO)_2{\cdot}4H_2O$ (100 mg) dissolved in 5 mL of methanol and denoted as Fe@ZIF-67 or Ni@ZIF-67, respectively. The bimetal Fe/Ni@ZIF-67 was prepared from ZIF-67 (200 mg) mixed with a solution of $Fe(CH_3COO)_2$ (50 mg) and $Ni(CH_3COO)_2{\cdot}4H_2O$ (100 mg) dissolved in methanol 10 mL. All suspensions were vigorously stirred at ambient conditions for 6 h before adding dispersed graphene oxide (GO, 78 mg in 10 mL methanol). Using sonication for 1 h, 24 h later, Fe@ZIF-67@GO or Ni@ZIF-67@GO or Fe/Ni@ZIF-67@GO was obtained, respectively. Additionally, graphene oxide (GO, 78 mg in 5 mL methanol) was directly mixed with a suspension of ZIF-67 (200 mg in 5 mL of methanol) as a reference sample (ZIF-67@GO). The suspensions were stirred at ambient temperature for 24 h. The solids were separated via centrifuge (9500 rpm for 10 min) and washed with cold methanol for one time before drying the samples at 50 °C under vacuum overnight. Finally, the dried solid samples were pyrolyzed at 600 °C using a programmable heating rate of 5 °C/min for 6 h under argon flow (20 cc/min) before cooling down to room temperature (samples denoted after pyrolysis: M-CoNC/RGO for ZIF-67 doped with Fe/Ni or both composited with GO).

Preparation of microwave samples (paraffin)

The microwave absorption experiment sample was provided in a ring shape with an outer diameter (OD) of 7.00 mm and an inner diameter (ID) of 3.04 mm. Well-mixed samples (20 mg of materials and 80 mg paraffin (binder)) were pressed into a toroidal-shaped customized mold to achieve standard size.

Preparation of composite materials in PDCPD

Fe/Ni-CoNC/RGO/PDCPD samples were synthesized using 100 mg Fe/Ni-CoNC/RGO mixing with 1.9 g of DCPD monomer (a drop of wetting agent GENAPOL(R) X-080 was added). The suspensions were sonicated at least 1 h before adding 2 μL of phenyl trichlorosilane (activator agent) and 1 mg of catalyst ((S-IMes)(2- [(2-methyl-phenylimino)methyl]-phenoxy)(3–2-methylphenyl-5-methyl-inden-1-ylidene)Ru(II)Cl (GMCX, China)) dissolved in dichloromethane. Then, those mixtures were poured into molds, which were pre-heated at 120 °C for 30 min. A carving machine (Wuhan Jiangpai Technology co., LTD, SJ-1325) was applied to cut out samples according to the standard size/shape as mentioned before.

2.3. Material characterizations

Powder X-ray diffraction (PXRD) patterns were analyzed using a Bruker D8 Advance X-ray diffractometer equipped with Cu-Kα sealed tube (λ = 1.542 Å), operated at 40 kV and 40 mA, at a scan velocity of 0.2 s/step, scanning step length of 0.02 ° / step from 5 to 80° Raman analyses were performed using a RENISHAW InVia Raman microscope with a Ne-He laser excitation operated at 633 nm wavelength. Fourier Transform infrared spectroscopy (FTIR) was performed using a Vertex 80v (Bruker, Germany). X-ray photoelectron spectroscopy (XPS) was performed on an ESCALAB 250Xi spectrometer.

Scanning electron microscopy (SEM) images and Energy-dispersive X-ray spectroscopy (EDS) were carried out on a MIRA3 TESCAN scan electron microscope operated at 20 kV. Transmission electron microscopy (TEM) image using a Cu grid was obtained by an FEI Tecnai G2F30 microscope and an accelerating voltage of 300 kV. The element content was confirmed by Prodigy 7 Inductively Coupled Plasma-Optical Emission Spectroscope (ICP-OES), wavelength range of 165~1100 nm, optical resolution 0.007 nm (at 200 nm), and analysis precision less than 2%. Magnetic properties of samples were acquired by a vibrating sample magnetometer (VSM, Lake Shore 7404) with an external magnetic field of −20,000 to 20,000 Oe at ambient temperature. The electromagnetic parameters were analyzed using a VNA, Agilent N5247A vector network analyzer in the frequency range of 2–18 GHz after a full two-port calibration (SHORT–OPEN–LOAD–THRU).

3. Results and discussion

3.1. Material characterization

High crystalline porous ZIF-67 was synthesized under ambient conditions (room temperature) since it is a fast and cost-effective method to produce this material, as shown in Scheme 1. The ligand (2-MIM) deprotonates and coordinates to metal ions (Co), forming a crystalline ZIF-67. The characterization of the obtained ZIF-67 revealed similar characteristic properties as previously reported. [26] For example, the powder X-ray diffraction (PXRD) pattern confirmed a high crystalline nature, perfectly matching the simulated structure, as shown in Fig. S2a. Scanning electron microscope (SEM) analyses revealed rhombic dodecahedron crystal morphologies and particle sizes ranging from 200 to 500 nm (Fig. S1b).

The ZIF-67 doped with Fe, Ni, or Fe/Ni ions, were synthesized, and after the doping, the crystal morphology was analyzed by SEM, as shown in Fig 1a. Due to the stirring of the suspension, leading to the partial break-down of ZIF particles, a particle size ranging from 150 to 500 nm was obtained. Next, the composite materials were synthesized based on doped ZIF (Fe@ZIF-67, Ni@ZIF-67, and Fe/Ni@ZIF-67) and graphene oxide (GO). The morphology of GO was characterized via SEM. A folded microstructure with a thin layer sheet-like structure, with particle sizes ranging from nanometer to micrometer, was observed (Fig. S1a). The Fe/Ni@ZIF-67@GO morphology was also identified by SEM, where Fe/Ni@ZIF-67 was anchored on the GO surface, as shown in Fig. 1b. Subsequently, the composite materials were pyrolyzed in a tubular furnace under Ar atmosphere at 600 °C for 6 h. A black-colored product was obtained after the pyrolysis process with a weight loss of ≈ 60%. Shrunken rhombic dodecahedral morphologies of the ZIF-67 shape were observed after pyrolysis, as shown in Fig. 1c. Fig. 1d demonstrates the metal element dispersion of Co, Fe, and Ni of the pyrolyzed material (Fe/Ni-CoNC/RGO), revealing that Co, Fe, and Ni elements are regularly dispersed. The metal content of Fe/Ni-CoNC/RGO was analyzed via SEM-EDS Mapping and Inductively Coupled Plasma-Optical Emission Spectroscopy (ICP-OES). The obtained results (Fig. 2g) show that the total contents of metals (bulk) are all higher than on the surface, indicating that most metals are present inside the pyrolyzed materials. The nanostructure of the synthesized material was investigated by high-resolution transmission electron microscopy (HR-TEM). The metal nanoparticles are implanted in the carbon matrix, as shown in Fig. 1e. Also, HR-TEM observed variance of lattice fringes (Fig. 1f, g). For example, the interplanar distance of 2.4 Å might be attributed to the [311] plane of Co_3O_4, while a distance of 2 Å might be assigned to the [111] plane of Co, the [110] plane of Fe, the [031] plane of Fe_3C or the [111]

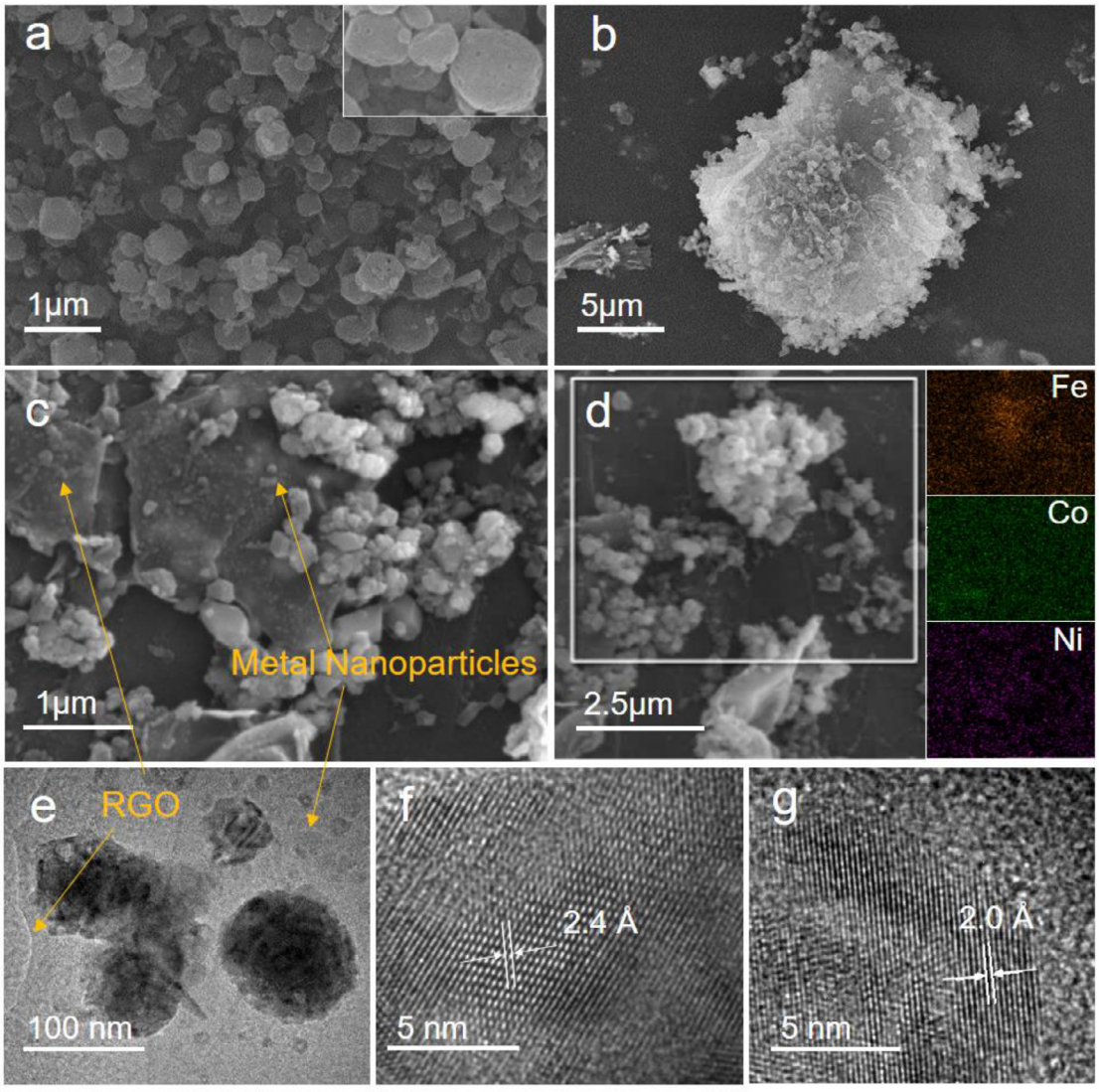

Fig. 1. SEM image of Fe/Ni@ZIF-67 (a), Fe/Ni@ZIF-67@GO (b), Fe/Ni-CoNC/RGO (c), element mapping of Fe/Ni-CoNC/RGO (SEM-EDS) (d), TEM image of Fe/Ni-CoNC/RGO (e), HR-TEM of metal nanoparticles (f, g) in sample Fe/Ni-CoNC/RGO.

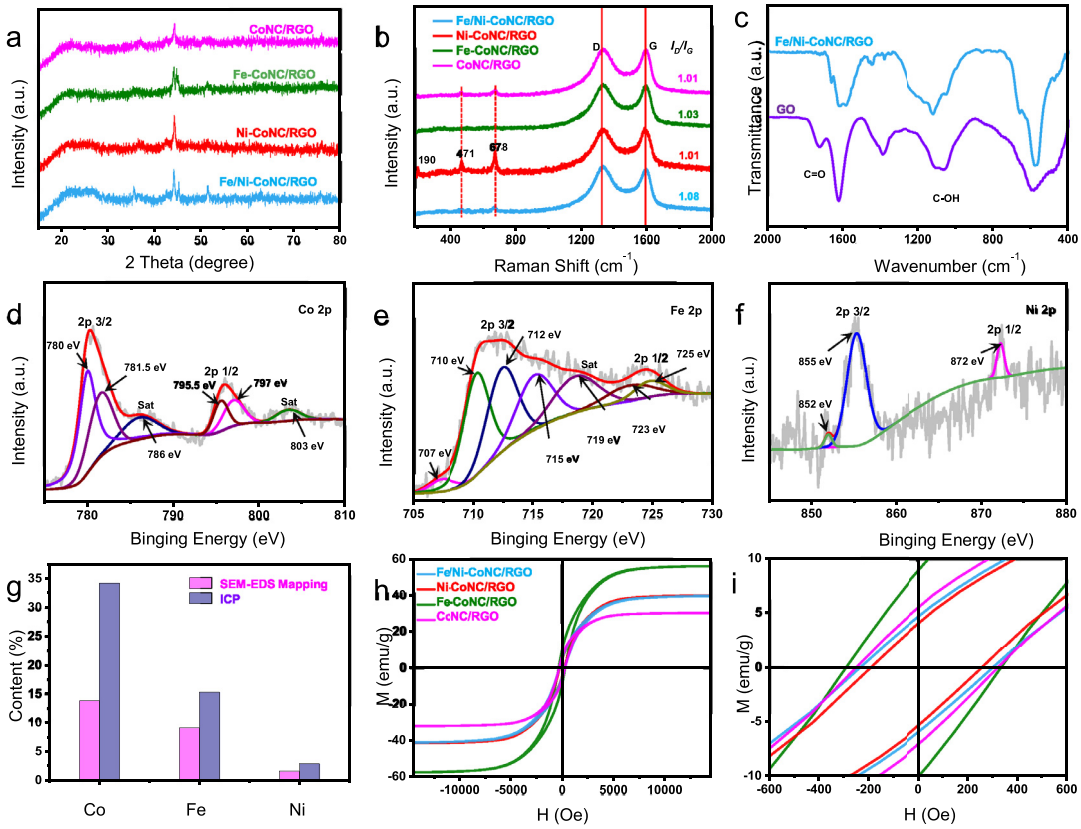

Fig. 2. The PXRD pattern (a) and Raman spectra (b) of CoNC/RGO, Fe-CoNC/RGO, Ni-CoNC/RGO, and Fe/Ni-CoNC/RGO, FT-IR spectra (c) of GO comparable to Fe/Ni-CoNC/RGO, Co 2p XPS spectra (d), Fe 2p XPS spectra (e), Ni 2p XPS spectra (f) of Fe/Ni-CoNC/RGO, SEM-EDS Mapping and ICP metal content results (g) of sample Fe/Ni-CoNC/RGO, VSM patterns (h) and partial enlarged VSM patterns (i) of CoNC/RGO, Fe-CoNC/RGO, Ni-CoNC/RGO, and Fe/Ni-CoNC/RGO.

plane of Ni [27]. Furthermore, these results suggest the reduction of GO to RGO and the decomposition of the ZIF-67 framework structure occur during the pyrolysis process, and metal nanoparticles of Co, Fe, and Ni are generated and well-dispersed in the carbon matrix structure.

Once the carbonaceous composited materials are prepared, the carbonaceous composited materials are mixed in the required ratio with paraffin or DCPD for wave absorption measurements (ratio sample/paraffin=20%; ratio sample/DCPD=5%; all ratios are the maximum filling amount of each absorber in the matrix). Subsequently, the mixtures are transferred into an appropriate mold to produce the final samples, Scheme 1.

The crystalline structure of the synthesized materials was verified by PXRD analysis. Firstly, the purchased GO was characterized and revealed a peak at 11.2° in the XRD spectrum corresponding to [001] carbon plane (Fig. S2b) with an interlayer space of 7.9 Å (Bragg equation $2d\sin\theta = n\lambda$; λ=1.542 Å) [28]. A decrease in size, crystallinity, and disorder of the graphene structure after a high-temperature treatment (pyrolysis) causes the crystal pattern change from GO to RGO [29]. In Fig.2a, the crystal pattern of pyrolyzed ZIF-67@GO reveals peaks at 2θ=44.2°, 51.5°, and 75.8° which originate from crystal planes of metallic β-Co (PDF #15−0806) at [111], [200], and [220], respectively. Additionally, the obvious diffraction peak at 36.8° is attributed to the crystal plane [311] of Co_3O_4 (PDF #43−1003). The Fe-doped materials (Fe-CoNC/RGO and Fe/Ni-CoNC/RGO) exhibited additional peaks at 2θ=44.7° and 65.0°, corresponding to Fe crystal planes [110] and [200] (PDF #06−0696). Moreover, an additional secondary phase related to the Fe_3C crystal plane [031] at 2θ=45.0° (PDF #65−2413) was also observed in the XRD pattern of the doped Fe samples. Samples containing Ni disclose Ni crystal (PDF #65−2865) peaks, situated close to the Co crystal peaks, at 2θ=44.5°, 51.8°, and 76.4° assigned to the planes [111], [200], and [220] respectively. Besides those peaks of the Ni crystal phase, the appearance of the $NiFe_2O_4$ (PDF #54−0964) crystal plane [311] at 2θ=35.7° in Fe/Ni-CoNC/RGO was also observed in the diffraction pattern. These data are consistent with TEM results that metal Fe, Co, or Ni, Fe_3C, and Co_3O_4 are present.

The presence of the metallic Co phase in the Fe/Ni-CoNC/RGO sample was also confirmed via Raman spectroscopy. The band set at 190 cm^{-1}, 471 cm^{-1}, and 678 cm^{-1} are assigned to the $F_{2g}^{(3)}$ mode, E_g symmetry mode, and A_{1g} symmetry mode of the crystalline metallic Co [30], respectively (Fig. 2b). The Raman analysis also provided more detailed structural information about the chemical speciation of carbon. The spectra of all materials revealed two cognizable peaks at 1334 and 1600 cm^{-1} assigned to D- and G-bands of the carbon species, respectively [31]. The G band is a characteristic feature of graphitic layers, whereas the D band corresponds to disordered carbon or defective graphitic structures. Hence, the ratio of the D- and G-band (I_D/I_G) integrated intensities from the Raman spectrum was used to assess the graphitization degree in the carbon materials. Firstly, the I_D/I_G ratio of GO and RGO are 0.94 and 0.98, respectively (Fig. S2c). The increasing value of I_D/I_G indicates that more sp^2 hybridization or defect carbon structures are generated after the pyrolysis process [32]. The pyrolyzed composite materials exhibit a growing I_D/I_G ratio comparable to non-composite (RGO). Higher sp^2 hybridization might result from carbon generated from the carbonized imidazole structures of ZIF-67. The I_D/I_G ratio was slightly different for each composite material; nevertheless, the highest value was observed for Fe/Ni-CoNC/RGO (Fig. 2b). Moderate graphitization degree or proper content of defects for carbon-based materials has been confirmed to be helpful for the attenuation of incident electromagnetic (EM) waves. This could improve the matched characteristic impedance

and prompt energy transition from contiguous states to Fermi level and introduce defect polarization relaxation and dipole relaxation.

Further information regarding the functional groups or chemical environment of the synthesized materials was obtained by Fourier Transform infrared spectroscopy (FTIR). In Fig. 2c, the vibration band at 1730 cm^{-1} is assigned to the $\nu_{C=O}$ stretch vibration of carbonyl groups in GO [33]. This vibration band drastically decreased for the Fe/Ni-CoNC/RGO but is still present. However, a new band at 575 cm^{-1} was observed in Fe/Ni-CoNC/RGO, representing the M-O (M=Co, Fe or Ni) stretch vibration. [34, 35] The combined results of TEM, XRD, and FTIR confirm the existence of metal oxides.

X-ray photoelectron spectroscopy (XPS) was applied for the surface analysis of Fe/Ni-CoNC/RGO to gain more insight regarding the chemical state and chemical bonding of the species present in the sample. All spectra were fitted after subtraction of the Shirley background. The C 1 s spectrum of precursor GO gave five peaks after deconvolution corresponding to C—C at 284.8 eV, C—OH at 285.5 eV, C—O at 286.2 eV, C = O at 287.6 eV, and O = C—O at 288.9 eV (Fig. S2d). The survey spectrum of Fe/Ni-CoNC/RGO (Fig. S2e) indicated the presence of the chemical species C, N, O, Co, Fe, and Ni. The deconvolution of the Co 2p spectrum revealed two doublets, one doublet for $Co^{III}2p_{3/2}-2p_{1/2}$ at 780 and 795.5 eV, the second doublet for Co^{II} $2p_{3/2}-2p_{1/2}$ at 781.5 and 797 eV [36]. Satellite peaks (Sat) for Co were also observed at 786 and 803 eV, as shown in Fig. 2d. [37] The Fe 2p spectrum [38] contains Fe^{II}, Fe^{III}, and Fe^{0}, with a doublet contribution of Fe^{II} (710, 723 eV) and of Fe^{III} (712, 725 eV). The values at 715 and 719 eV are assigned to satellite peaks (Sat) for Fe^{II} and Fe^{III}. A small contribution of Fe^{0} can be found at 707 eV (Fig. 2e) [39]. Fig. 2f displays the binding energies at 852 eV and at 855/872 eV, which can be assigned to metallic nickel [40] Ni^{0} and Ni^{II}, respectively. For the Ni^{0}, the Ni $2p_{1/2}$ is masked and consequently not visible. Most of the nickel present in the material is Ni^{II} and a small amount exists as metallic Ni. Furthermore, the C 1 s, N 1 s and O 1 s spectra of the synthesized Fe/Ni-CoNC/RGO exhibit peaks of C—C (284.8 eV), C = N (285.9 eV), C—O (286.9 eV), C = O (288.9 eV), C = C (291.9 eV), pyridinic-N (398.9 eV), Co-N (399.8 eV), pyrrolic-N (401.1 eV), graphitic-N (402.6 eV), oxidized-N (404.6 eV), and O^{2-} (530.1 eV) as shown in Fig. S2f-h. [41] Particularly, the N-species derived from pyrolyzed 2-MIM are reported to be beneficial to constitute open reticular carbon walls/matrix and tune the electrical properties [42]. The latter is advantageous to obtain stronger and broader bandwidth wave absorption of electromagnetic radiation. Moreover, different N-structures also affect wave absorption properties differently. Pyrrolic-/pyridinic-N is primarily required for the dipolar relaxation loss, while graphitic-N is favorable for conduction loss. The XPS results demonstrate the presence of the different oxidation states for the elements, which is consistent with the species detected by XRD.

The hysteresis loops [43] of the magnetic materials CoNC/RGO, Fe-CoNC/RGO, Ni-CoNC/RGO, and Fe/Ni-CoNC/RGO composites at room temperature are depicted in Fig. 2h, i. The static magnetic properties of these composite samples are given in Table 1. The addition of Ni

Table 1
Magnetic properties of the prepared samples.

Sample	Ms (emu/g)	Mr (emu/g)	Hc (Oe)
CoNC/RGO	31.09	6.31	288.00
Fe-CoNC/RGO	56.70	9.50	314.12
Ni-CoNC/RGO	40.57	4.72	226.32
Fe/Ni-CoNC/RGO	40.20	5.33	269.86

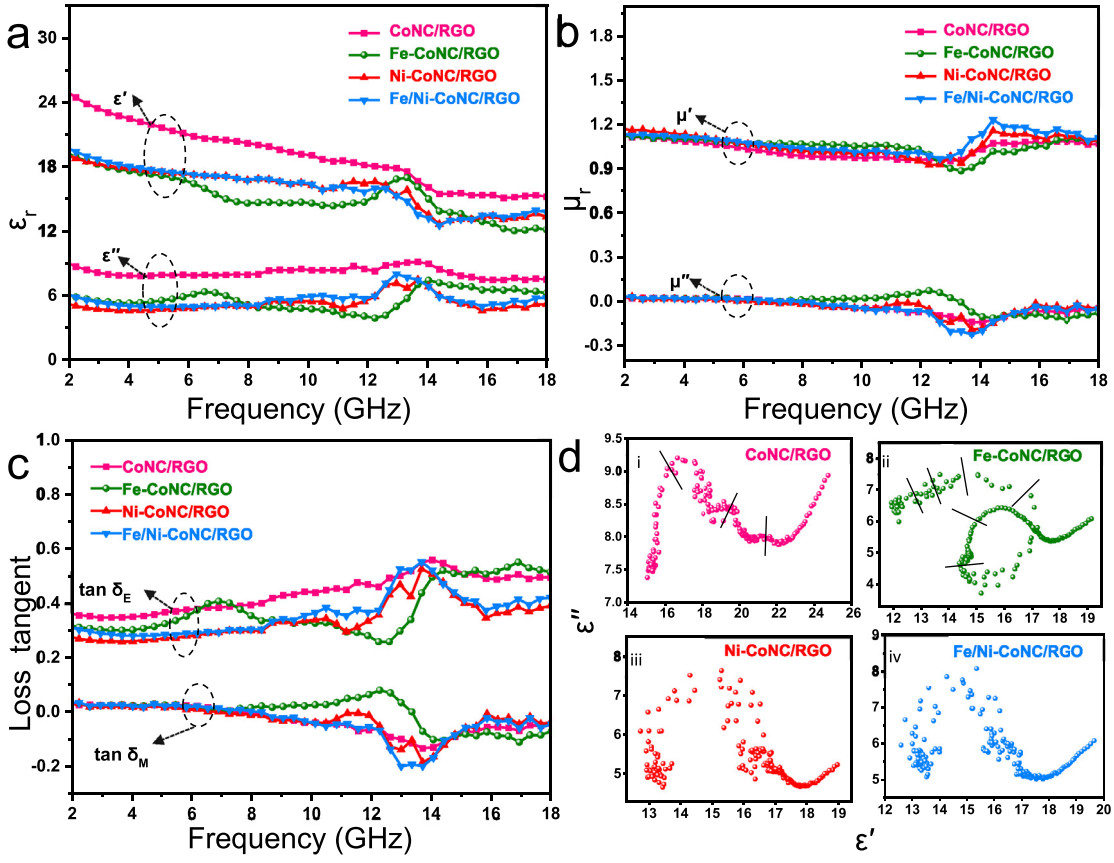

Fig. 3. Frequency dependence of the electromagnetic parameters for CoNC/RGO, Fe-CoNC/RGO, Ni-CoNC/RGO, and Fe/Ni-CoNC/RGO. (a) the real part (ε') and imaginary part (ε'') of complex permittivity, (b) the real part (μ') and imaginary part (μ'') of complex permeability, (c) the dielectric tangent loss and the magnetic tangent loss, (d) Cole-Cole plots.

and Fe elevated the saturation magnetization (Ms) property. Especially the addition of high saturation magnetism iron metal increased the values of Ms, remanent magnetization (Mr), and coercive field (Hc) for Fe-CoNC/RGO composite resulting in the highest observed values. This high value of saturation magnetization is usually conducive to high-frequency resonance [44].

3.2. Microwave absorption

Electromagnetic absorption properties greatly rely on the complex permittivity ($\varepsilon_r = \varepsilon' - j\varepsilon''$) and complex permeability ($\mu_r = \mu' - j\mu''$). The real part (ε') of the complex permittivity is a variable of the polarization intensity under the action of an external electric field, representing its ability to store energy. In contrast, the imaginary part (ε'') of the complex permittivity is the energy consumption caused by the rearrangement of the electric couple moment under the action of an external electric field. The real part (μ') of the complex permeability is energy storage produced under the action of an external magnetic field. In contrast, the complex permeability's imaginary part (μ'') is the energy loss of an external magnetic field [45]. Furthermore, electron polarization, internal dipole polarization [46], ionic polarization, interfacial polarization [47], interface and multiple scattering [48], exchange resonance, natural resonance [49], magnetic hysteresis, eddy current loss, domain wall resonance loss, etc., can influence permittivity and permeability.

Fig. 3 shows that the electromagnetic parameters of the four microwave absorbents depend on the frequency. ε' values (Fig. 3a) generally show a declining trend with rising of the frequency probably caused by the decline in space charge polarization with frequency raising [50], while ε'' values (Fig. 3a) fluctuate at a particular range. Compared with CoNC/RGO, the ε', ε'', and calculated dielectric tangent loss [51] ($\tan\delta_E = \varepsilon''/\varepsilon'$, Fig. 3c) values of the samples containing Ni or Fe are lower. This results from the existence of extra magnetic metal species, which are available to reduce dielectric performance and obtain well electromagnetic impedance matching. Interfacial polarization was enhanced by different phases and increased interface area. Obviously, peaks can be seen in permittivity curves; they may come from dipole polarization or interfacial polarization [52] among RGO and metal components. The conductivity loss was generated by a conductive network afforded by a hierarchical carbon Co-N matrix and free electrons emanating from metal-containing nanoparticles. The existence of conductivity loss can also be confirmed by the line tail in Cole-Cole plots (Fig. 3d) according to Eq. S1 [53]. At the same time, the distinguishable semicircles in the plots confirmed the Debye relaxation processes. Furthermore, the distorted semicircles imply that other loss mechanisms also exist in these composite systems.

The μ' values (Fig. 3b) of the four samples fluctuate within the selected frequency range. Meanwhile, due to the highest magnetic properties, the Fe-CoNC/RGO sample shows the highest μ'' value (Fig. 3b) and magnetic tangent loss ($\tan\delta_M = \mu''/\mu'$, Fig. 3c) at a specific frequency range. Furthermore, the μ'' graph shows the minimum value is −0.22; these negative μ'' suggests that the composites radiated out a magnetic energy. [54] The resonance peaks of permeability values in the high-frequency part are mainly owing to exchange resonance [55, 56].

Based on the above electromagnetic parameter values and using Eq. S2 and Eq. S3, the reflection loss maps were constructed [57, 58] (Fig. 4). Fig. 4a, b exhibits the calculated absorbing result for CoNC/RGO. An effective absorption in the frequency band from 3.4 to 4.2 GHz shows a maximum absorption of −16.8 dB with a thickness of 4 mm. The widest effective absorption [59] in the frequency band from 10.7 to 13.2 GHz illustrates a maximum absorption of −15.6 dB with a thickness of 1.5 mm. For this sample, with different thicknesses, the gaps of maximum absorption are small. Fig. 4c, d displays the calculated absorbing result for Fe-CoNC/RGO; the sample shows strong absorption in the low-frequency range and large thickness region, the strongest absorption with maximum absorption of −33.9 dB at 5.0 mm is realized. In the high-frequency range and thin thickness region, a broad absorption from 11.6 to 15.2 GHz with maximum absorption of −24.7 dB at a thin thickness of 1.5 mm is observed. Fig. 4f, g displays the calculated absorbing result for Ni-CoNC/RGO; this sample has strong attenuation in the high-frequency range and thin thickness region. As the frequency increases and the thickness decreases, the absorbing properties show a broadband absorption, from 11.3 to 15.0 GHz with a maximal absorption of −38.7 dB at a thin thickness of 1.5 mm. Fig. 4h, i displays the calculated absorption for Fe/Ni-CoNC/RGO. Combining the advantages of Fe-CoNC/RGO and Ni-CoNC/RGO samples, an excellent absorption intensity and width is obtained from 6.5 to 8.1 GHz with maximum absorption of −51.6 dB with a thickness of 2.5 mm. The widest effective absorption from 11.5 to 14.5 GHz of −42.4 dB with the thickness of 1.5 mm, can be perceived. In Fig.4e, it is shown that sample Fe/Ni-CoNC/RGO possess the maximum absorption with appropriate thickness and effective bandwidth. Impedance matching Z_{in}/Z_0 [60] (Fig. S3) stands for balancing the complex permittivity and permeability, the tri-metal sample Fe/Ni-CoNC/RGO achieved the best impedance matching, its real part of Z_{in}/Z_0 is the closest to 1, and the imaginary part is the nearest to 0. This may benefit from the formation of $NiFe_2O_4$ nanoparticles [61]. Attenuation constant α [62] (Eq. S4) represents the decay of electromagnetic waves inside the samples; in general, all the attenuation constants (Fig. S4a) are all increased with raised frequency. If C_0 values [63] (Eq. S5) remain constant, this implies that the eddy current loss plays an essential role in the magnetic loss. However, C_0 values (Fig. S4b) vary with the frequency, indicating that resonances functioned in the magnetic loss [64]. As a result, the bimetal sample exhibits the best microwave absorption properties among these four samples. A recent literature survey of the microwave absorption performances of various absorbents in paraffin is given in table S1.

Having this excellent microwave absorbing material in hand, which is still a powder, there is a need to composite this material straightforwardly to be applied in real applications. We selected dicyclopentadiene (DCPD) as a monomer, of which the mechanical and thermal properties are provided in Table S2. Dicyclopentadiene (DCPD) can be used as a monomer and produces polymers in high yield. Polymerization of the DCPD by a ruthenium catalyst through ring-opening metathesis polymerization (ROMP) generates a thermoset polymer called polydicyclopentadiene (PDCPD). This polymer can be tailored to satisfy divergent material requirements, leading to a wide range of applications in automobiles, aerospace, ballistics, sport and recreation, microelectronics, etc. DCPD is a monomer with low viscosity, making it easy to obtain a homogeneous mixture of the microwave absorbing material with DCPD.

Furthermore, the monomer's viscosity increases with an increasing amount of additive (graphene or RGO); hence, only a small amount can be well dispersed in the DCPD monomer. Once a homogeneous mixture of the microwave absorbing material with DCPD was obtained, the ruthenium catalyst was added. The mixture was injected into the mold, and polymerization occurred, so the microwave absorbent material was incorporated in the poly-DCPD matrix (PDCPD). This procedure is similar to reaction injection molding (RIM), a well-known industrial process used to polymerize DCPD [65–67].

After the polymerization process, the final sample was investigated for its microwave absorbing properties and for the effect of compounding in a PDCPD matrix. Fig. 5 displays the electromagnetic parameters of the polymer samples as a function of the frequency. Fig. 5a depicts the real part and the imaginary part of the permittivity. Distinctly declined ε' values together with increased ε'' values with frequency, resulted in uptrend dielectric tangent loss (Fig. 5d). μ'

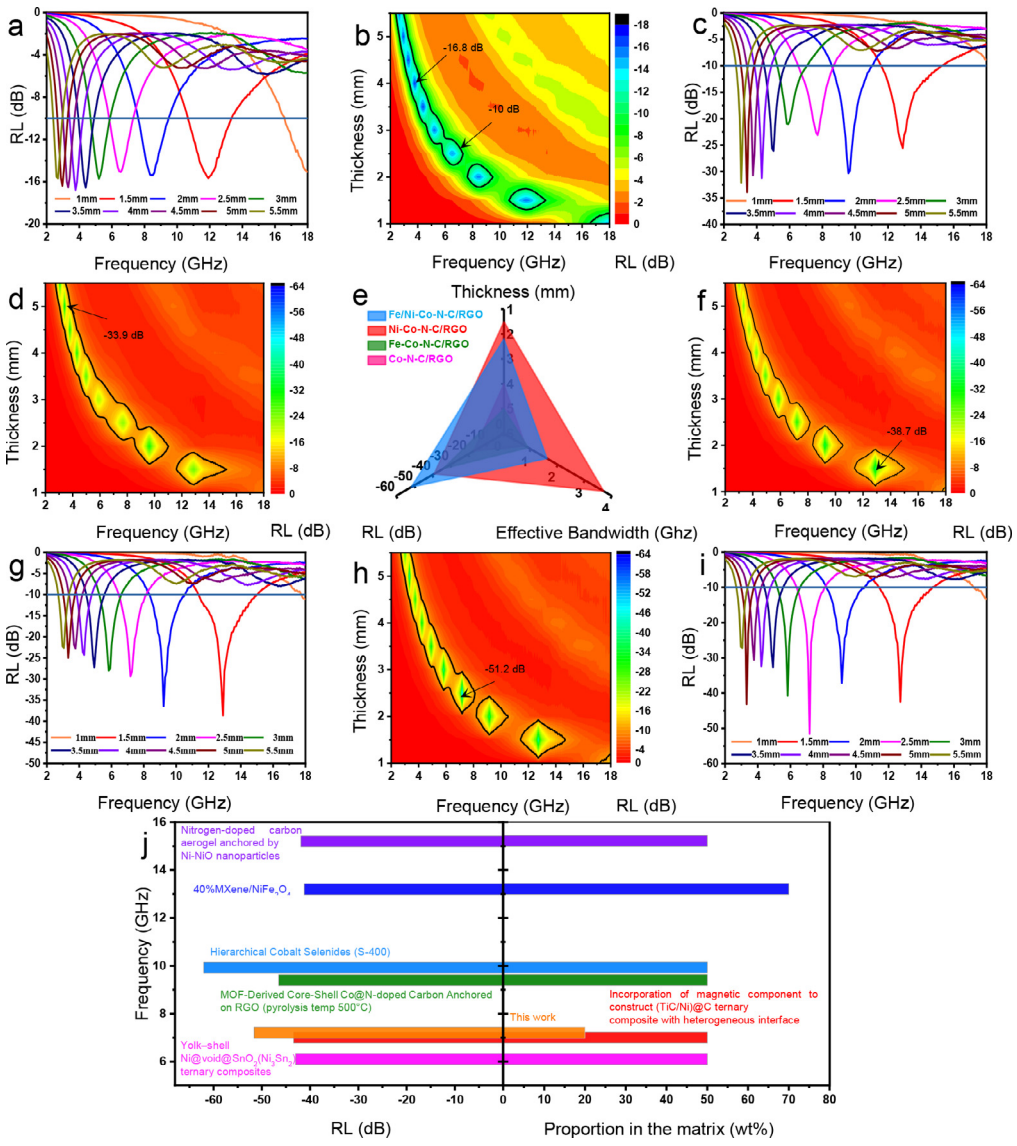

Fig. 4. Reflection loss for four different samples: CoNC/RGO (a) and (b); Fe-CoNC/RGO (c) and (d); (e) the relationship among thickness, RL and effective bandwidth of all the samples, the electromagnetic wave absorption performance; Ni-CoNC/RGO (f) and (g); Fe/Ni-CoNC/RGO (h) and (i); (j) Fe/Ni-CoNC/RGO absorber compared with other Co, Fe, Ni containing materials.

values (Fig. 5b) show a simple harmonic shape, while μ'' reveals resonance peaks at low frequency [68], this phenomenon may originate from natural resonance [69]. Combining tan δ_E and tan δ_M results (Fig. 5c) reveal that the microwave absorption property of this polymer sample relies on magnetic tangent loss in the low frequency and dielectric tangent loss in the high frequency range.

The reflection losses for the mentioned polymer samples are depicted in Fig. 5c; the maximum absorption with a thin thickness of 1.5 mm is −24.5 dB. The widest effective absorption frequency bands vary from 10.3 GHz to 14.1 GHz with maximum absorption of −21.9 dB with a thickness of 2 mm. The absorbing curves changed with the frequency and absorber's thickness. The strongest absorption peaks remarkably shift to the low frequency direction with increasing thickness, in agreement with the quarter-wavelength cancelation model (Fig. 5f). The relationship between the frequency shift and thickness for the maximum microwave absorption was expressed in Eq. S6. Specifically, when the phase difference between the incident and reflected waves in the microwave absorber equals π [70], then the waves will cancel each other at the air-absorber interface. Undoubtedly, the experimental values matched well with the simulated quarter-wave curve. This excellent microwave absorption property is not only due to the notable good impedance matching (Fig. S5a,b) but also due to the high attenuation constant (Fig. 5e) [71]. The C_0 values (Fig. 5e) still all vary with frequency, indicating that not only eddy current loss make efforts for the absorption property. Especially the peaks in the low-frequency part again prove the existence of natural resonance. A literature survey of the microwave absorption performances of various absorbents in different polymer matrixes is given in Fig. 4j, and detailed information is supported in Table.S1.

Based on the above investigation, Fe/Ni doped cobalt-nitrogen-carbon matrix on RGO can meaningfully enhance microwave absorption, broaden the bandwidth and reduce the absorption thickness. Due to the best impedance balance, the incident wave can enter into the absorber with seldom a portion of reflection. After the entrance, various attenuation models (Scheme. 2) help to convert and consume the microwave energy. Three types of polarization may exist in this system:

1. Defect carbon structures in RGO and the defects in the crystal structure may cause defect polarization.

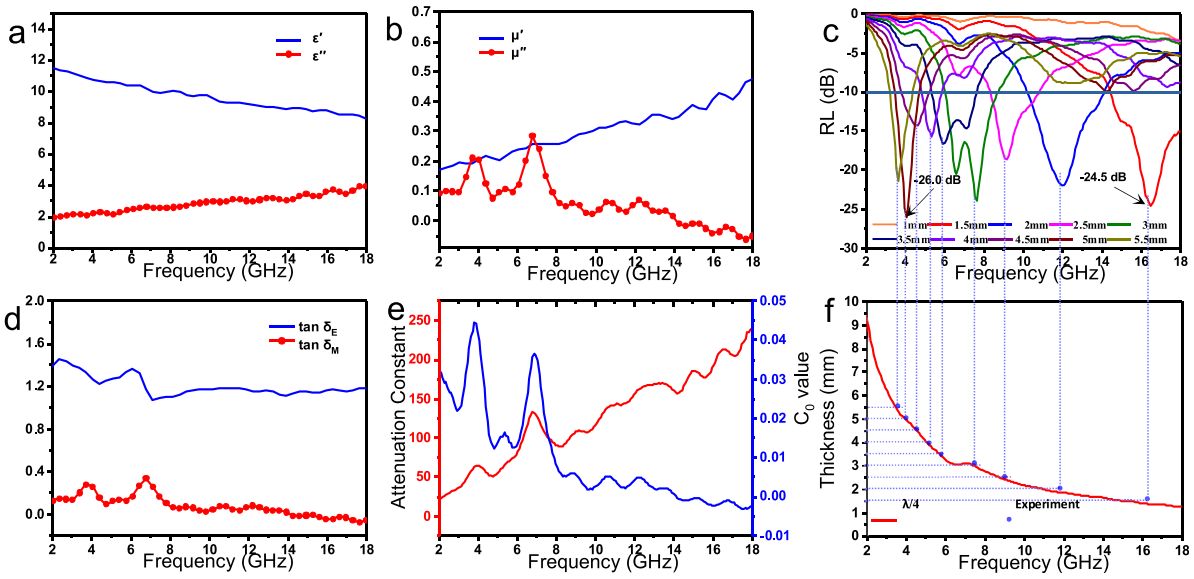

Fig. 5. Frequency dependence of electromagnetic parameters Fe/Ni-CoNC/RGO/PDCPD. Complex permittivity (a), complex permeability (b), reflection loss (c), the dielectric tangent loss and the magnetic tangent loss (d), attenuation constant and C0 value (e), dependence of the matching thickness on frequency under $\lambda/4$ (f).

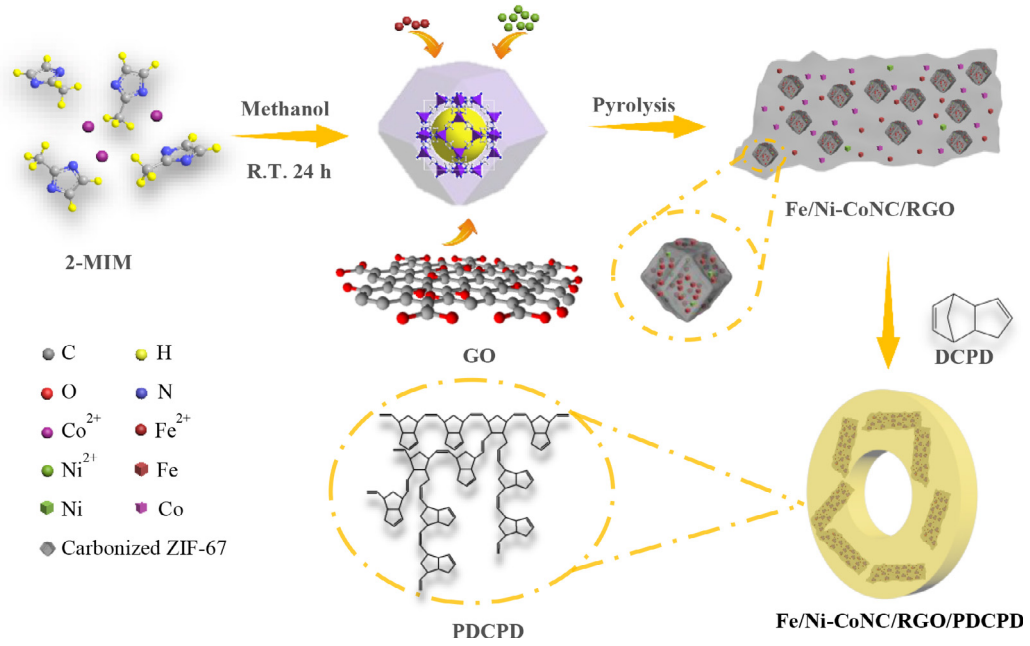

Scheme 1. Schematic illustration of the process for the synthesis Fe/Ni-CoNC/RGO/PDCPD.

2. When inherent dipoles in asymmetric molecules respond to the applied electric field, dipolar polarization happens.

3. Due to the charge accumulation, interfacial polarization happened at the interface of the heterogeneous media (RGO, metallic nanoparticle, cobalt-nitrogen-carbon, and matrix).

The energy consumed by the migration and hopping of electrons in the conductive network is the conductivity loss.

The magnetic loss generally derives from natural resonance, exchange resonance, and eddy current loss. Eddy current loss is generated when the conductors move in a non-uniform magnetic field or appear in a magnetic field varied with time. Only the external alternating current (AC) magnetic field can cause natural resonance in this system due to the anisotropic magnetic field inside. In the end, if the incident wave runs into its counterpart of the opposite phase from the reflection, optimized absorption performance can be created.

4. Conclusion

An effective and efficient microwave absorbent was developed by introducing the desired amount of magnetic (Fe/Ni) doping material in a cobalt-nitrogen-carbon matrix on RGO. Magnetic Fe and Ni nanoparticles, especially $NiFe_2O_4$, optimize the impedance matching of Fe/Ni-CoNC/RGO composites, generating excellent reflection loss performance over the whole selected frequency range. Owing to the excellent dielectric and magnetic properties, together with the optimal impedance matching, −51.6 dB of 7.2 GHz can be obtained at a thin thickness of 2.5 mm. The results demonstrate that MOF materials,

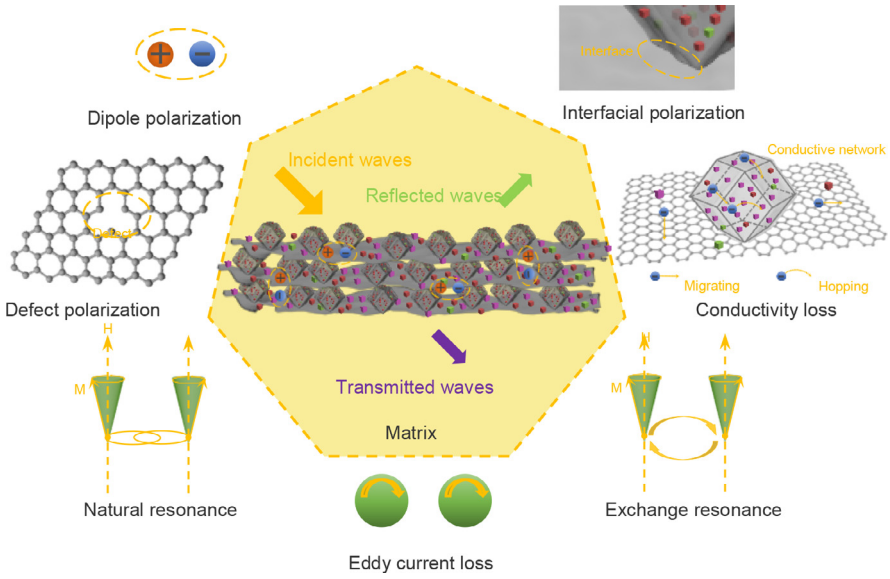

Scheme 2. A possible schematic illustration of microwave attenuation models in the Fe/Ni-CoNC/RGO/PDCPD.

together with metal oxides nanoparticles or metal nanoparticles anchored on RGO, can generate good absorbing properties. Based on such an excellent microwave absorbent, the resulting Fe/Ni-CoNC/RGO/PDCPD composite reached −24.5 dB at 16.5 GHz with a thickness of 1.5 mm, achieving outstanding impedance matching, interfacial polarization, defect polarization, and natural resonance, increasing its attenuation ability. The present work shines the light on the multimetal and multicomponent design of microwave absorption materials.

Declaration of Competing Interest

The authors declare no known competing financial interests or personal relationships that could have appeared to influence the work reported in this paper.

CRediT authorship contribution statement

Qi Chen: Investigation, Writing – original draft. **Xiaogang Su:** Investigation. **Xing Liu:** Investigation. **Jichao Wang:** Investigation. **Rongguo Song:** Investigation. **Daping He:** Investigation. **Somboon Chaemchuen:** Funding acquisition, Writing – review & editing. **Francis Verpoort:** Visualization, Writing – review & editing, Supervision.

Acknowledgements

The authors are grateful to the State Key Lab of Advanced Technology for Materials Synthesis and Processing for financial support (Wuhan University of Technology). S.C. acknowledges the support of the National Natural Science Foundation of China (No.21850410449).

Supplementary materials

Supplementary material associated with this article can be found in the online version at doi:10.1016/j.jtice.2022.104350.

References

[1] Yuan J, Liu Q, Li S, Lu Y, Jin S, Li K, Chen H, Zhang H. Metal organic framework (MOF)-derived carbonaceous Co_3O_4/Co microframes anchored on RGO with enhanced electromagnetic wave absorption performances. Synth Met 2017;228:32–40 http://doi.org/10.1016/j.synthmet.2017.03.020.

[2] Xu HL, Yin XW, Li MH, Ye F, Han MK, Hou ZX, et al. Mesoporous carbon hollow microspheres with red blood cell like morphology for efficient microwave absorption at elevated temperature. Carbon N Y 2018; 132:343–51 http://doi.org/10.1016/j.carbon.2018.02.040.

[3] Zhou YL, Muhammad J, Zhou TH, Wang DX, Wang X, Duan YP, Zhang XF, Dong XL, Zhang ZD. Incorporation of magnetic component to construct (TiC/Ni)@C ternary composite with heterogeneous interface for enhanced microwave absorption. J Alloys Compd 2019;778:779–86 http://doi.org/10.1016/j.jallcom.2018.11.237.

[4] Zhang N, Liu XD, Huang Y, Wang MY, Li S, Zong M, Liu P. Novel nanocomposites of cobalt ferrite covalently-grafted on graphene by amide bond as superior electromagnetic wave absorber. J Colloid Interface Sci 2019;540:218–27 http://doi.org/10.1016/j.jcis.2019.01.025.

[5] Hassan HMA, Abdelsayed V, Khder AERS, AbouZeid KM, Terner J, El-Shall MS, Al-Resayes SI, El-Azhary AA. Microwave synthesis of graphene sheets supporting metal nanocrystals in aqueous and organic media. J Mater Chem 2009;19 http://doi.org/10.1039/b906253j.

[6] Ensafi AA, Rezaloo F, Rezaei B. $CoFe_2O_4$/reduced graphene oxide/ionic liquid modified glassy carbon electrode, a selective and sensitive electrochemical sensor for determination of methotrexate. J Taiwan Inst Chem Eng 2017;78:45–50 http://doi.org/10.1016/j.jtice.2017.05.031.

[7] Wang J, Yang F, Wang S, Zhong H, Wu ZK, Cao ZF. Reactivation of nano-Fe_3O_4/diethanolamine/rGO catalyst by using electric field in Fenton reaction. J Taiwan Inst Chem Eng 2019;99:113–22 http://doi.org/10.1016/j.jtice.2019.03.009.

[8] Ruttanapun C, Phrompet C, Tuichai W, Karaphun A, Daengsakul S, Sriwong C. Influence of free electron charge and free extra framework anions in calcium aluminate@ rGO (CA@ rGO) cement composites with enhanced dielectric and electrochemical properties. J Taiwan Inst Chem Eng 2021;127:334–48 http://doi.org/10.1016/j.jtice.2021.08.007.

[9] Wu Y, Shu RW, Li ZY, Guo CL, Zhang GY, Zhang JB, Li WJ. Design and electromagnetic wave absorption properties of reduced graphene oxide/multi-walled carbon nanotubes/nickel ferrite ternary nanocomposites. J Alloys Compd 2019;784:887–96 http://doi.org/10.1016/j.jallcom.2019.01.139.

[10] Liu LL, Wang L, Li QQ, Yu XF, Shi XF, Ding JJ, You WB, Yang LT, Zhang YH, Che RC. High-performance microwave absorption of MOF-derived core-shell Co@N-doped carbon anchored on reduced graphene oxide. Chem Nano Mat 2019;5:558–65 http://doi.org/10.1002/cnma.201800637.

[11] Jiao SQ, Wu MZ, Yu XX, Zhang H. Enhanced Microwave Absorption: the Composite of Fe_3O_4 Flakes and Reduced Graphene Oxide with Improved Interfacial Polarization. Adv Eng Mater 2020;22 http://doi.org/10.1002/adem.201901299.

[12] Yan J, Huang Y, Liu XD, Zhao XX, Th Li, Zhao Y, Liu PB. Polypyrrole-based composite materials for electromagnetic wave absorption. Polym Rev 2021;61:646–87 http://doi.org/10.1080/15583724.2020.1870490.

[13] Zeng XJ, Cheng XY, Yu RH, Stucky GD. Electromagnetic microwave absorption theory and recent achievements in microwave absorbers. Carbon N Y 2020; 168:606–23 http://doi.org/10.1016/j.carbon.2020.07.028.

[14] Jiao ZM, Qiu J. Microwave absorption performance of iron oxide/multiwalled carbon nanotubes nanohybrids prepared by electrostatic attraction. J Mater Sci 2017;53:3640–6 http://doi.org/10.1007/s10853-017-1770-6.

[15] Yan J, Huang Y, Yan YH, Ding L, Liu PB. High-performance electromagnetic wave absorbers based on two kinds of nickel-based MOF-Derived Ni@C microspheres. ACS Appl Mater Interfaces 2019;11:40781–92 http://doi.org/10.1021/acsami.9b12850.

[16] Yan J, Huang Y, Yan YH, Zhao XX, Liu PB. The composition design of MOF-derived Co-Fe bimetallic autocatalysis carbon nanotubes with controllable

electromagnetic properties. Compos Part A 2020;139 http://doi.org/10.1016/j.compositesa.2020.106107.
[17] Qiu F, Wang ZY, Liu M, Wang ZM. Ding S, Synthesis, characterization and microwave absorption of MXene/$NiFe_2O_4$ composites. Ceram Int 2021;47:24713–20 http://doi.org/10.1016/j.ceramint.2021.05.194.
[18] Hassan HMA, Betiha MA, Mohamed SK, El-Sharkawy EA, Ahmed EA. Salen- Zr(IV) complex grafted into amine-tagged MIL-101(Cr) as a robust multifunctional catalyst for biodiesel production and organic transformation reactions. Appl Surf Sci 2017;412:394–404 http://doi.org/10.1016/j.apsusc.2017.03.247.
[19] Cao XH, Tan CL, Sindoro M, Zhang H. Hybrid micro-/nano-structures derived from metal−organic frameworks: preparation and applications in energy storage and conversion. Chem Soc Rev 2017;46:2660–77 http://doi.org/10.1039/c6cs00426a.
[20] Liu W, Liu L, Yang ZH, Xu JJ, Hou YL, Ji GB. A versatile route toward the electromagnetic functionalization of metal−organic framework-derived three-dimensional nanoporous carbon composites. ACS Appl Mater Interfaces 2018;10:8965–75 http://doi.org/10.1021/acsami.8b00320.
[21] Yan J, Huang Y, Han XP, Gao XG, Liu PB. Metal organic framework (ZIF-67)-derived hollow CoS_2/N-doped carbon nanotube composites for extraordinary electromagnetic wave absorption. Compos B Eng 2019;163:67–76 http://doi.org/10.1016/j.compositesb.2018.11.008.
[22] Shu RW, Wu Y, Li WJ, Zhang JB, Liu Y, Shi JJ, Zheng MD. Fabrication of ferroferric oxide−carbon/reduced graphene oxide nanocomposites derived from Fe-based metal−organic frameworks for microwave absorption. Compos Sci Technol 2020;196 http://doi.org/10.1016/j.compscitech.2020.108240.
[23] Li XL, Raza S, Liu CK. Enhanced photo-catalytic efficiency through dual-functional ZIF based materials: fabrication and application as a degradation of organic dyes. J Taiwan Inst Chem. Eng 2021;120:368–80 http://doi.org/10.1016/j.jtice.2021.03.022.
[24] Nataraj N, Chen T-W, Chen SM, Tseng T-W, Bian Y, Sun TT, Jiang JZ. Metal-organic framework (ZIF-67) interwoven multiwalled carbon nanotubes as a sensing platform for rapid administration of serotonin. J Taiwan Inst Chem Eng 2021;129:299–310 http://doi.org/10.1016/j.jtice.2021.09.034.
[25] Lu YY, Wang YT, Li HL, Lin Y, Jiang ZY, Xie ZX, Kuang Q, Zheng LS. MOF-Derived Porous Co/C Nanocomposites with Excellent Electromagnetic Wave Absorption Properties. ACS Appl Mater Interfaces 2015;7:13604–11 http://doi.org/10.1021/acsami.5b03177.
[26] Zhou K, Mousavi B, Luo ZX, Phatanasri S, Chaemchuen S, Verpoort F. Characterization and properties of Zn/Co zeolitic imidazolate frameworks vs. ZIF-8 and ZIF-67. J Mater Chem A 2017;5:952–7 http://doi.org/10.1039/c6ta07860e.
[27] Shen YQ, Wei YP, Ma JQ, Li QL, Li J, Shao WJ, Yan PZ, Huang GW, Du XY. Tunable microwave absorption properties of nickel-carbon nanofibers prepared by electrospinning. Ceram Int 2019;45:3313–24 http://doi.org/10.1016/j.ceramint.2018.10.242.
[28] Wu Q, Zhang H, Zhou LC, Bao C, Zhu H, Zhang YM. Synthesis and application of rGO/$CoFe_2O_4$ composite for catalytic degradation of methylene blue on heterogeneous Fenton-like oxidation. J Taiwan Inst Chem Eng 2016;67:484–94 http://doi.org/10.1016/j.jtice.2016.08.004.
[29] Wang Y, Du YC, Qiang R, Tian CH, Xu P, Han XJ. Interfacially Engineered Sandwich-Like rGO/Carbon Microspheres/rGO Composite as an Efficient and Durable Microwave Absorber. Adv Mater Interfaces 2016;3 http://doi.org/10.1002/admi.201500684.
[30] Li XB, Yang SW, Sun J, He P, Pu XP, Ding GQ. Enhanced electromagnetic wave absorption performances of Co_3O_4 nanocube/reduced graphene oxide composite. Synth Met 2014;194:52–8 http://doi.org/10.1016/j.synthmet.2014.04.012.
[31] Wan YT, Ye J, Wang LL, Dai JD. Interfacial engineering for ultrafine Co_3O_4 confined in graphene macroscopic microspheres with boosting peroxymonosulfate activation. J Taiwan Inst Chem Eng 2021;127:248–58 http://doi.org/10.1016/j.jtice.2021.08.024.
[32] Yan J, Huang Y, Wei C, Zhang N, Liu PB. Covalently bonded polyaniline/graphene composites as high-performance electromagnetic (EM) wave absorption materials. Compos. Part A 2017;99:121–8 http://doi.org/10.1016/j.compositesa.2017.04.016.
[33] Dung NT, Trang TT, Thao VD, Thu TV, Tung NQ, Huy NN. Enhanced degradation of organic dyes by peroxymonosulfate with Fe_3O_4-$CoCO_3$/rGO hybrid activation: a comprehensive study. J Taiwan Inst Chem Eng 2022;133 http://doi.org/10.1016/j.jtice.2022.104279.
[34] Kumar A, Bhattacharyya S. Porous NiFe-Oxide Nanocubes as Bifunctional Electrocatalysts for Efficient Water-Splitting. ACS Appl Mater Interfaces 2017;9:41906–15 http://doi.org/10.1021/acsami.7b14096.
[35] Jiao KL, Jiang Y, Kang ZP, Peng RY, Jiao SQ, Hu ZQ. Three-dimensional Co_3O_4@MWNTs nanocomposite with enhanced electrochemical performance for nonenzymatic glucose biosensors and biofuel cells. R Soc Open Sci 2017 (4):170991 http://doi.org/10.1098/rsos.170991.
[36] Hao JX, Peng SL, Qin TF, Wang ZL, Wen YX, He DY, Zhang JC, Zhang ZY, Fan XY, Cao GZ. Fabrication of hybrid Co_3O_4/$NiCo_2O_4$ nanosheets sandwiched by nanoneedles for high-performance supercapacitors using a novel electrochemical ion exchange. Sci China Mater 2017;60:1168–78 http://doi.org/10.1007/s40843-017-9139-8.
[37] Wang HF, Tang C, Wang B, Li BQ, Zhang Q. Bifunctional Transition Metal Hydroxysulfides: room-Temperature Sulfurization and Their Applications in Zn-Air Batteries. Adv Mater 2017;29 http://doi.org/10.1002/adma.201702327.
[38] Ganesan P, Sivanantham A, Shanmugam S. Inexpensive electrochemical synthesis of nickel iron sulphides on nickel foam: super active and ultra-durable electrocatalysts for alkaline electrolyte membrane water electrolysis. J Mater Chem A 2016;4:16394–402 http://doi.org/10.1039/c6ta04499a.
[39] Li Y, Xu J, Feng T, Yao QF, Xie JP, Xia H. Fe_2O_3 Nanoneedles on ultrafine nickel nanotube arrays as efficient anode for high-performance asymmetric supercapacitors. Adv Funct Mater 2017;27 http://doi.org/10.1002/adfm.201606728.
[40] Dong CQ, Kou TY, Gao H, Peng ZQ, Zhang ZH. Eutectic-derived mesoporous Ni-Fe-O nanowire network catalyzing oxygen evolution and overall water splitting. Adv Energy Mater 2018;8 http://doi.org/10.1002/aenm.201701347.
[41] Bao L, Li T, Chen S, Peng C, Li L, Xu Q, Chen YS, Ou EC, Xu WJ. 3D graphene frameworks/Co_3O_4 composites electrode for high-performance supercapacitor and enzymeless glucose detection. Small 2017;13 http://doi.org/10.1002/smll.201602077.
[42] Wang Y, Gao X, Wu XM, Zhang WZ, Luo CY, Liu PB. Facile design of 3D hierarchical $NiFe_2O_4$/N-GN/ZnO composite as a high performance electromagnetic wave absorber. Chem Eng J 2019;375 http://doi.org/10.1016/j.cej.2019.121942.
[43] Liu Y, Li Y, Jiang KD, Tong GX, Lv TX, Wu WH. Controllable synthesis of elliptical Fe_3O_4@C and Fe_3O_4/Fe@C nanorings for plasmon resonance-enhanced microwave absorption. J Mater Chem C 2016(4):7316–23 http://doi.org/10.1039/c6tc01737a.
[44] Liu PJ, Yao ZJ, Zhou JT, Yang ZH, Kong LB. Small magnetic Co-doped NiZn ferrite/graphene nanocomposites and their dual-region microwave absorption performance. J Mater Chem C 2016;4:9738–49 http://doi.org/10.1039/c6tc03518c.
[45] Zhao B, Guo XQ, Zhao WY, Deng JS, Fan BB, Shao G, Bai ZY, Zhang R. Facile synthesis of yolk−shell Ni@void@SnO_2(Ni_3Sn_2) ternary composites via galvanic replacement/Kirkendall effect and their enhanced microwave absorption properties. Nano Res 2016;10:331–43 http://doi.org/10.1007/s12274-016-1295-3.
[46] Liu PB, Yq Zhang, Yan J, Huang Y, Xia L, Guang ZX. Synthesis of lightweight N-doped graphene foams with open reticular structure for high-efficiency electromagnetic wave absorption. Chem Eng J 2019;368:285–98 http://doi.org/10.1016/j.cej.2019.02.193.
[47] Liu L, He N, Wu T, Hu PB, Tong GX. Co/C/Fe/C hierarchical flowers with strawberry-like surface as surface plasmon for enhanced permittivity, permeability, and microwave absorption properties. Chem Eng J 2019;355:103–8 http://doi.org/10.1016/j.cej.2018.08.131.
[48] Qin M, Lan D, Wu GL, Qiao XG, Wu HJ. Sodium citrate assisted hydrothermal synthesis of nickel cobaltate absorbers with tunable morphology and complex dielectric parameters toward efficient electromagnetic wave absorption. Appl Surf Sci 2020;504 http://doi.org/10.1016/j.apsusc.2019.144480.
[49] Zhang YL, Wang XX, Cao MS. Confinedly implanted $NiFe_2O_4$-rGO: cluster tailoring and highly tunable electromagnetic properties for selective-frequency microwave absorption. Nano Res 2018;11:1426–36 http://doi.org/10.1007/s12274-017-1758-1.
[50] Zhang R, Huang XX, Zhong B, Xia L, Wen GW, Zhou Y. Enhanced microwave absorption properties of ferroferric oxide/graphene composites with a controllable microstructure. RSC Adv 2016;6:16952–62 http://doi.org/10.1039/c5ra22254k.
[51] Green M, Liu ZQ, Xiang P, Liu Y, Zhou MJ, Tan XY, Huang FQ, Liu L, Chen XB. Doped, conductive SiO_2 nanoparticles for large microwave absorption. Light: Sci Appl 2018;7:87 http://doi.org/10.1038/s41377-018-0088-8.
[52] Liu QW, Zeng M, Liu J, Guo BY, Hao XZ, Cao Q, et al. Fe-based material@N-doped carbon composites as environment-friendly microwave absorbers. Carbon N Y 2021; 171:646–57 http://doi.org/10.1016/j.carbon.2020.09.045.
[53] Wang HG, Meng FB, Huang F, Jing CF, Li Y, Wei W, Zhou ZW. Interface modulating CNTs@PANi hybrids by controlled unzipping of the walls of CNTs to achieve tunable high-performance microwave absorption. ACS Appl Mater Interfaces 2019;11:12142–53 http://doi.org/10.1021/acsami.9b01122.
[54] Xu DW, Yang S, Chen P, Yu Q, Xiong XH, Wang J. 3D nitrogen-doped porous magnetic graphene foam-supported Ni nanocomposites with superior microwave absorption properties. J Alloys Compd 2019;782:600–10 http://doi.org/10.1016/j.jallcom.2018.12.239.
[55] Lan D, Qin M, Yang RS, Chen S, Wu HJ, Fan YC, Fu QH, Zhang FL. Facile synthesis of hierarchical chrysanthemum-like copper cobaltate-copper oxide composites for enhanced microwave absorption performance. J Colloid Interface Sci 2019;533:481–91 http://doi.org/10.1016/j.jcis.2018.08.108.
[56] Meng FB, Wang HG, Wei Chen ZJ, Li T, Li CY, Xuan Y, Zhou ZW. Generation of graphene-based aerogel microspheres for broadband and tunable high-performance microwave absorption by electrospinning-freeze drying process. Nano Res 2018;11:2847–61 http://doi.org/10.1007/s12274-017-1915-6.
[57] Green M, Tian L, Xiang P, Murowchick J, Tan XY, Chen XB. FeP nanoparticles: a new material for microwave absorption. Mater. Chem. Front 2018;2:1119–25 http://doi.org/10.1039/c8qm00003d.
[58] Yu Y-H, Ma C-CM, Yu K-C, Teng C-C, Tien H-W, Chang K-Y, Kuo Y-K. Preparation, morphological, and microwave absorbing properties of spongy iron powders/epoxy composites. J Taiwan Inst Chem Eng 2014;45:674–80 http://doi.org/10.1016/j.jtice.2013.05.005.
[59] ur Rehman S, Wang JM, Luo QH, Sun MZ, Jiang L, Han Q, Liu JC, Bi H. Starfish-like C/$CoNiO_2$ heterostructure derived from ZIF-67 with tunable microwave absorption properties. Chem Eng J 2019;373:122–30 http://doi.org/10.1016/j.cej.2019.05.040.
[60] Quan B, Xu GY, Gu WH, Sheng JQ, Ji GB. Cobalt nanoparticles embedded nitrogen-doped porous graphitized carbon composites with enhanced microwave absorption performance. J Colloid Interface Sci 2019;533:297–303 http://doi.org/10.1016/j.jcis.2018.08.083.
[61] Cao Y, Mohamed AM, Mousavi M, Akinay Y. Poly(pyrrole-co-styrene sulfonate)-encapsulated MWCNT/Fe−Ni alloy/$NiFe_2O_4$ nanocomposites for microwave absorption. Mater. Chem. Phys 2021;259 http://doi.org/10.1016/j.matchemphys.2020.124169.
[62] Song ZM, Liu XF, Sun X, Li Y, Nie XY, Tang WK, et al. Alginate-templated synthesis of CoFe/carbon fiber composite and the effect of hierarchically porous structure

on electromagnetic wave absorption performance. Carbon N Y 2019; 151:36–45 http://doi.org/10.1016/j.carbon.2019.05.025.
[63] Huang L, Liu XF, Yu RH. An efficient Co/C microwave absorber with tunable Co nanoparticles derived from a ZnCo bimetallic zeolitic imidazolate framework. Part Part Syst Charact 2018;35 http://doi.org/10.1002/ppsc.201800107.
[64] Li ZN, Han XJ, Ma Y, Liu DW, Wang YH, Xu P, Li CL, Du YC. MOFs-Derived Hollow Co/C Microspheres with Enhanced Microwave Absorption Performance. ACS Sustain. Chem Eng 2018;6:8904–13 http://doi.org/10.1021/acssuschemeng.8b01270.
[65] Allaert B, Dieltiens N, Ledoux N, Vercaemst C, Van Der Voort P, Stevens CV, Linden A, Verpoort F. Synthesis and activity for ROMP of bidentate Schiff base substituted second generation Grubbs catalysts. J Mol Catal A: Chem 2006;260:221–6 http://doi.org/10.1016/j.molcata.2006.07.006.
[66] Monsaert S, Lozano Vila A, Drozdzak R, Van Der Voort P, Verpoort F. Latent olefin metathesis catalysts. Chem. Soc. Rev 2009;38:3360–72 http://doi.org/10.1039/b902345n.
[67] Monsaert S, Ledoux N, Drozdzak R, Verpoort F. A highly controllable latent ruthenium Schiff base olefin metathesis catalyst: catalyst activation and mechanistic studies. J Polym Sci Part A: Polym Chem 2010;48:302–10 http://doi.org/10.1002/pola.23784.
[68] Liu XF, Hao CC, He LH, Yang C, Chen YB, Jiang CB, Yu RH. Yolk−shell structured Co-C/Void/Co_9S_8 composites with a tunable cavity for ultrabroadband and efficient low-frequency microwave absorption. Nano Res 2018;11:4169–82 http://doi.org/10.1007/s12274-018-2006-z.
[69] Wu Y, Shu RW, Zhang JB, Sun RR, Chen Y, Yuan J. Oxygen vacancy defects enhanced electromagnetic wave absorption properties of 3D net-like multi-walled carbon nanotubes/cerium oxide nanocomposites. J Alloys Compd 2019;785:616–26 http://doi.org/10.1016/j.jallcom.2019.01.227.
[70] Zeng M, Cao Q, Liu J, Guo BY, Hao XZ, Liu QW, Liu XF, Sun X, Zhang XX, Yu RH. Hierarchical cobalt selenides as highly efficient microwave absorbers with tunable frequency response. ACS Appl Mater Interfaces 2020;12:1222–31 http://doi.org/10.1021/acsami.9b15172.
[71] Cheng Y, Li ZY, Li Y, Dai SS, Ji GB, Zhao HQ, et al. Rationally regulating complex dielectric parameters of mesoporous carbon hollow spheres to carry out efficient microwave absorption. Carbon N Y 2018; 127:643–52 http://doi.org/10.1016/j.carbon.2017.11.055.